Measurement of the double K-shell vacancy creation probability in the electron-capture decay of ^{55}Fe with active-pixel detectors

Thilo Michel,[1,*] Benedikt Bergmann,[2] Jürgen Durst,[3] Mykaylo Filipenko,[1] Thomas Gleixner,[1] and Kai Zuber[4]

[1]*Erlangen Centre for Astroparticle Physics (ECAP), Friedrich-Alexander-Universität Erlangen-Nürnberg, Erwin-Rommel-Str. 1, 91058 Erlangen, Germany*

[2]*Institute for Experimental and Applied Physics, Czech Technical University in Prague, Horska 3a/22, 128 00 Praha 2, Czech Republic*

[3]*Faculty of Physics, Ludwig-Maximilians-Universität München, Schellingstr. 4, 80799 München, Germany*

[4]*Institut für Kern-und Teilchenphysik, Technische Universität Dresden, Zellescher Weg 19, 01068 Dresden, Germany*

(Received 15 October 2013; revised manuscript received 22 November 2013; published 13 January 2014)

Background: In electron-capture decay, a second K-shell vacancy is eventually created with a small probability. Measurements of the double-vacancy creation probability per K-shell electron capture P_{KK} of various nuclei undergoing electron-capture decays have already been performed, but the statistical accuracy of P_{KK} of several nuclides is still not satisfying.

Purpose: The purpose of this experiment was to improve the statistical error of P_{KK} in the decay of ^{55}Fe and to demonstrate the possibility of detecting double-vacancy creation events with position resolving pixel detectors. This enables angle resolved measurements.

Method: For the first time, two active-pixel detectors (A,B) were used to detect satellite- and hypersatellite-line photons in coincidence either both in two clusters of triggered pixels in only one detector (A,B) or in both detectors (A $\wedge$ B). P_{KK} was determined for the two detectors regarded as one single, larger detector (P_{KK}), for each detector separately (single-sided analysis: $P_{KK,\mathrm{A}\veebar\mathrm{B}}$), and for both detectors in coincidence (double-sided analysis: $P_{KK,\mathrm{A}\wedge\mathrm{B}}$).

Results: The result of the experiment is $P_{KK} = (1.531 \pm 0.079) \times 10^{-4}$ with a systematic error of $(\Delta P_{KK})_{\mathrm{syst}} = \pm 0.023 \times 10^{-4}$. This value is in agreement with the value previously measured by Campbell *et al.* of $P_{KK} = (1.3 \pm 0.2) \times 10^{-4}$. The discrepancy in literature between P_{KK} of ^{54}Mn to the expected value extrapolated from ^{55}Fe almost vanished with our result. The asymmetry between the result of the single-sided analysis ($P_{KK,\mathrm{A}\veebar\mathrm{B}}$) and the double-sided analysis ($P_{KK,\mathrm{A}\wedge\mathrm{B}}$) is consistent with zero: $(P_{KK,\mathrm{A}\veebar\mathrm{B}} - P_{KK,\mathrm{A}\wedge\mathrm{B}})/(P_{KK,\mathrm{A}\veebar\mathrm{B}} + P_{KK,\mathrm{A}\wedge\mathrm{B}}) = -0.003 \pm 0.051$. This supports the assumption that angular correlations between the two photons are negligible within the achieved level of statistical accuracy for the given angular acceptance of our detectors.

Conclusions: One can conclude that hybrid photon counting pixel detectors can be used to measure angular correlations between the directions of emission of satellite and hypersatellite photons. Our result supports the suspicion that the reported discrepancy between P_{KK} measured for the electron-capture decays of ^{54}Mn and ^{55}Fe was probably due to statistical fluctuations in the measurements. Furthermore, the Z^{-2} dependence of P_{KK} predicted by Primakoff and Porter is supported. The improved statistical error of our measurements underlines the previously reported discrepancy between P_{KK} expected for ^{65}Zn if an extrapolation is carried out from our result on ^{55}Fe. Thus, our result strengthens the need for triple coincidence measurements of P_{KK} on ^{65}Zn.

DOI: 10.1103/PhysRevC.89.014609 PACS number(s): 23.40.−s, 27.40.+z, 32.80.Aa, 32.80.Zb

I. INTRODUCTION

In K-shell electron-capture decays, the remaining K-shell electron can be promoted to a higher energy level (shake-up) or can (mostly) be ejected from the daughter atom (shake-off) thus leaving an atom with an empty K shell. This double-vacancy creation process has a small probability of about 10^{-5}–10^{-3} per K capture and arises due to the sudden change in the electrostatic potential [1] of the nucleus and the change of the screening strength for the nuclear charge by the captured electron. The contribution of the shake-up process to this probability is negligible [2]. In theoretical predictions of the probability (P_{KK}) for this process, overlap integrals of the involved electron wave functions in the initial and final states of all partners are calculated. Thus, the double-vacancy production probability measures electron-electron correlations. Ideally, all electrons of the atomic shells are considered for an exact calculation. The higher the charge of the decaying nucleus, the more important a correct relativistic treatment of the wave functions becomes. Thus, precise measurements of P_{KK} help to understand the physics of multielectron systems and their numerical description.

The first observation of double-vacancy production following K-shell electron capture was reported by Charpak [3]. $P_{KK} = (3.8 \pm 1.7) \times 10^{-4}$ was measured with gaseous detectors for ^{55}Fe. The probabilities of double-vacancy production P_{KK} per K-shell electron capture have already been measured for various nuclei: ^{37}Ar [4], ^{54}Mn [1,5], ^{55}Fe [2,3,6], ^{65}Zn [7], ^{71}Ge [8], ^{85}Sr [9], ^{88}Y [10], ^{103}Pd [11], ^{109}Pd [12], ^{109}Cd [12], ^{113}Sn [13], ^{125}I [14], ^{131}Cs [15], ^{139}Ce [16], ^{165}Er [17], ^{181}W [17], ^{207}Bi [18]. Table IV in the publication of Hindi and Kozub [14] gives an overview on the measured values for P_{KK} in electron-capture decays.

*Corresponding author: Thilo.Michel@physik.uni-erlangen.de

In all these measurements of P_{KK} in electron-capture decays with energy-resolving detectors, except in the experiments of Campbell *et al.* [2] and Charpak [3], two nonpixelated NaI, Si(Li), or germanium detectors with high detection efficiency on two sides of radioactive sources were operated in coincidence, eventually in coincidence with a third detector for γ-ray detection from excited states of the daughter nucleus. With the triple coincidence technique, the generation of a second K-shell vacancy by internal conversion could be excluded from calculation of P_{KK} for some nuclei which decay to excited states of the daughter nucleus. Double-vacancy creation was usually identified by analyzing the recorded energy spectra for the tiny emission lines corresponding to the hypersatellite and satellite energies. Hypersatellite photons are generated in the transition $1s^{-2} \rightarrow 1s^{-1}2p^{-1}$ of the electron shell of the daughter atom. Satellite photons are emitted during the transition $1s^{-1}2p^{-1} \rightarrow 2p^{-2}$ of the electron shell of the daughter atom.

To the best of our knowledge, Campbell *et al.* [2] performed the only measurement of P_{KK} on a nuclide undergoing electron capture with a single-sided setup employing a single lithium drifted silicon detector. They were able to demonstrate that P_{KK} in the electron-capture decay of ^{55}Fe to ^{55}Mn can be determined from the emitted photon energy spectrum close to the Kβ_{13} diagram line of the daughter atom. Diagram line photons are emitted in filling of a vacancy without presence of a second vacancy. Their result depended on the exact knowledge of the energy response of the detector. P_{KK} was extracted from the line strength of the $K\beta$ hypersatellite. The $K\alpha$ hypersatellite remained invisible in the energy spectra. They stated a value of $P_{KK} = (1.3 \pm 0.2) \times 10^{-4}$ which agreed with the value $P_{KK} = (1.2 \pm 0.4) \times 10^{-4}$ measured before by Briand *et al.* [6] in a double-sided coincidence setup with two Si(Li) detectors facing each other with the source between them. The P_{KK} value measured by Campbell *et al.* has the smallest error for ^{55}Fe in literature.

Hindi and Kozub [14] stated that further improvements in the experimental accuracy were needed in order to refine the theoretical models to predict P_{KK}. There is a discrepancy between P_{KK} for ^{55}Fe and two nuclides with similar nuclear charge Z, namely, ^{54}Mn and ^{65}Zn, whose experimental P_{KK} values have been measured to be P_{KK} (^{54}Mn)$= 2.5^{+0.8}_{-0.5} \times 10^{-4}$ by Hindi, White, and Kozub [1] and P_{KK}(^{65}Zn)$= (2.2 \pm 0.2) \times 10^{-4}$ by Nagy and Schupp [7]. These results for ^{54}Mn and ^{65}Zn are both too high by a factor of $1.636^{+0.622}_{-0.436}$ (^{54}Mn) and 2.253 ± 0.403 (^{65}Zn) with respect to the value of P_{KK} which is expected with Z^{-2} extrapolation, predicted by Primakoff and Porter [19], to the nuclear charges of Mn and Zn from the value measured by Campbell *et al.* for ^{55}Fe. A reason might be that ^{54}Mn and ^{65}Zn both decay to excited states with subsequent γ emission in contrast to ^{55}Fe which decays almost always to the ground state of ^{55}Mn. To resolve this, Hindi, White, and Kozub [1] used a triple coincidence technique to eliminate contributions from internal conversion in the decay of ^{54}Mn. Their result was still 1.64 standard deviations larger than the value that would be expected from extrapolation of the result of Campbell *et al.* on ^{55}Fe if the uncertainties of both measurements were taken into account. Looking at the measured P_{KK} values given above, it becomes clear that there is still the need for higher precision data in order to be able to draw the right conclusions. It is a motivation of this work to reduce the statistical error on P_{KK} of ^{55}Fe in a double-sided setup.

All experiments to measure P_{KK} on electron-capture nuclides assume [20] that there is no angular correlation between the momenta of the hypersatellite and satellite photons. As far as we know, this assumption has never been tested, probably due to the long measuring times needed to measure P_{KK} even over the full solid angle which is due to the small probability of double-vacancy production and the large background from random coincidences. Angular correlations are typically sensitive to admixtures of higher electric or magnetic moments of the transition radiations between the involved states in the atomic shells. A measurement of P_{KK} and the angular correlations between the satellite and hypersatellite photons can test the treatment of relativistic quantum electrodynamics in models of multielectron systems. It is another motivation of this work to demonstrate that angular correlations between hypersatellite and satellite photons can be measured with a reasonable effort with the next generation hybrid counting pixel detectors. The analysis described here is completely different to earlier measurements of double-vacancy production probabilities because it does not exploit energy measurements.

Furthermore, this work demonstrates that the approach to use hybrid pixel detectors to detect the neutrino-accompanied double electron capture presented by Cermak *et al.* [21] is promising. The signal of the neutrino-accompanied double electron capture is similar to the signal after double-vacancy creation following single electron capture: two fluorescence photons are emitted from the daughter atom at the same time.

The time resolving hybrid pixel detectors like the Timepix detectors [22] might open a new era in the measurement of angular correlations between particles with energies of more than approximately 3.5 keV. It will be shown that despite their drawback of a worse energy resolution (compared to monolithic germanium or silicon drift detectors), the measurement of weak signals, whose signatures differ only slightly in energy from random background, is possible. In fact, in the specific operation mode of the Timepix detector that was used here, no energy information was used about the individual photons, except that their energy must have been larger than the discriminator threshold of approximately 3 keV. This limitation is due to the electronics architecture of the pixel detector Timepix, which allows either the recording of the energy deposition or the recording of the moment of detection via time stamping.

At a first glance, it seems to be impossible to extract a double-vacancy production probability of $\approx 10^{-4}$ per K-shell electron capture with this kind of detector because of the inferior energy resolution compared to germanium, or Si(Li), detectors. However, it will be shown that it is indeed possible because of the fine segmentation of the detector in combination with a moderate time resolution. This opens the possibility for future angular correlation measurements.

II. MATERIALS AND METHODS

A. Experimental setup

The $(3/2)^-$ ground-state nucleus of ^{55}Fe decays mainly to the $(5/2)^-$ ground state of ^{55}Mn via electron capture with a Q value of 231.21(18) keV and a half-life of $T_{1/2} = 2.747(8)$ yr [23]. The second forbidden decay to the excited $(7/2)^-$ state of ^{55}Fe with subsequent photon emission with 105.26(18) keV occurs with a probability of 1.3×10^{-7}%. K-shell electron capture occurs with a probability of $P_K = 88.53(16)$%, whereas an L-shell electron is captured with $P_L = 9.83(13)$%. An M-shell electron is captured in $P_M = 1.63(8)$% of the decays. The relaxation of the electronic shell of the daughter atom ^{55}Mn is accompanied by K-fluorescence photon emission in 28.42% [23] of all decays or by emission of Auger electrons. The K-fluorescence yield is $\omega_K = 0.321$. The energies of the K lines of manganese are $K\alpha_1 = 5.88765$ keV, $K\alpha_2 = 5.89875$ keV, $K\beta_3 = 6.49045$ keV, and $K\beta_5'' = 6.5352$ keV [23].

Figure 1 shows a sketch of the compact experimental setup. Two Timepix [22] hybrid active-pixel detectors (named detector A and detector B, labeled 2A and 2B in Fig. 1) were positioned with PVC holders (labeled 5 in Fig. 1) on two sides of a radioactive ^{55}Fe source (labeled 4 in Fig. 1). The p-in-n silicon sensor layers of the detectors were facing the source. The readout electronics printed circuit boards (labeled 1 in Fig. 1) with the detectors were oriented vertically in the laboratory in order to reduce the rate of high energy particles from cosmic rays traversing both detectors.

The Timepix detectors were comprised of 300-μm-thick p-in-n silicon sensors with distances of 55 μm between the 256 $\times$ 256 p implants which formed the sensor pixel electrodes. The pixels were organized in a matrix of 256 rows and 256 columns with an active area of 1.4 $\times$ 1.4 cm^2. The silicon sensor was fully depleted with an electric potential difference of 100 V between the common electrode (facing the source) and the sensor pixel electrodes. With these bias conditions and the doping scheme of the sensor, the holes which are released by ionizing particles in the sensitive pixel volume drift towards the pixel electrodes. They influence

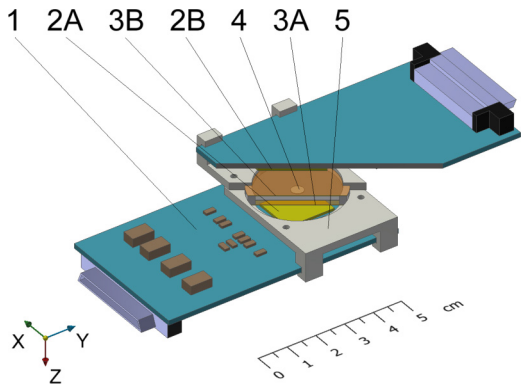

FIG. 1. (Color online) The experimental setup comprised readout electronics printed circuit board (1), Timepix detectors A and B (2A, 2B), Kapton foils for electron attenuation (3A, 3B) on both sides of the radioactive source (4). The structure was held together with a PVC holder (5).

currents in the pixel electrodes due to their drift motion [24,25]. Each sensor pixel is connected via under-bump metallization and a metal bump bond to the input electrode of an electronics cell in the Timepix application-specific integrated circuit (ASIC). The Timepix has been developed by the Medipix collaboration [26,27] in cooperation with the EUDET project in IBM 0.25 μm CMOS technology. In each pixel cell, the influenced current is converted to a voltage pulse by a charge sensitive amplifier. The maximum possible preamplifier gain was chosen for our measurements. The peaking time of the preamplifier output pulse was about $t_{\text{rise}} = 90$ ns [22]. The length of the falling edge of the amplifier output pulse is in the order of microseconds, depending on the energy deposited in the pixel. This voltage pulse is compared to a globally adjustable threshold by a leading-edge discriminator in each pixel. The minimum threshold that can be realized with negligible amount of noise-induced triggering of pixels is approximately 3 keV. The equivalent noise charge of the preamplifier output amounts to 110 electrons (rms) which corresponds to about 380-eV energy loss of a charged particle in silicon. The following signal processing is only digital and depends on the operation mode of the pixel which is chosen. Each pixel can be configured in one of three modes of digital operation. In the counting mode, the discriminator generates a digital pulse, which is used to increment a 14-bit pseudorandom counter in the pixel cell. The number of events above threshold is counted until the external shutter stops the digital activity. The period with enabled digital activity is called the frame time. In the time-over-threshold mode, the discriminator generates a digital pulse whose length equals the period during which the output signal of the preamplifier is above threshold. This period is correlated to the energy deposited in the pixel. In each triggered pixel, the pseudorandom counter registers the number of coincidences between periodic digital clock signals and the discriminator output pulse. By counting pulses of a clock with known frequency, the length of the time above threshold and thus deposited energy is determined in each triggered pixel. In the time-of-detection mode, the counting of clock cycles once started by exceeding the discriminator threshold does not stop until the external shutter is closed. In this mode, which was used for the measurements presented here, the counter value represents the time between the moment of detection and the closing of the external shutter. Clock frequencies of $f_{\text{fine}} = 48$ MHz and $f_{\text{coarse}} = 9.6$ MHz were used. No further events are recorded after the shutter is closed. The pseudorandom counters in each column of the pixel matrix then act as shift registers to transfer the digital information in the counters to the periphery on the ASIC. The data are shifted bit after bit via a serial link to the Fitpix readout [28] which is connected via a USB port to the data acquisition computer. A readout-clock frequency of 80 MHz was used for all measurements. The software PIXELMAN [29] controlled the detectors and data storage. A dedicated NIM electronics was set up for synchronization of the frames of the two detectors. The external shutters of the two detectors were opened simultaneously with a precision of better than 20 ns using a NIM gate generator after both detectors had finished their readout. The gate generator also closed the shutters simultaneously after 232 μs (measurements

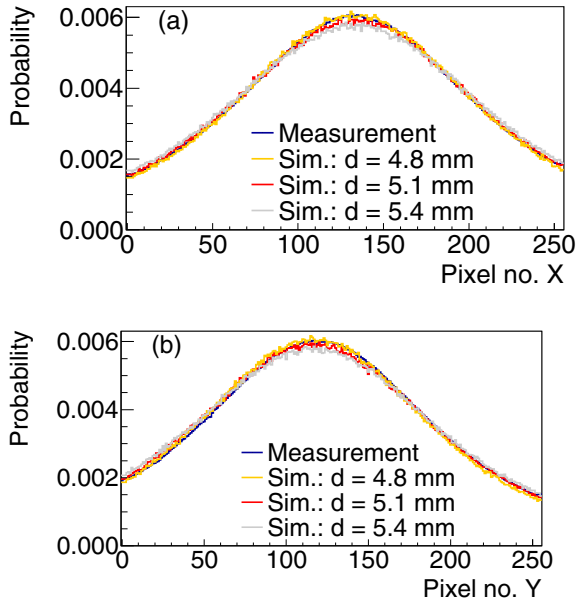

FIG. 2. (Color online) Detector A: Measured and simulated distributions of the points of detection (a) projected to the x axis (detector rows) in Fig. 1, and (b) projected to the y axis (detector columns) in Fig. 1. The simulations (Sim.) were carried out for different distances d between the source and detector A.

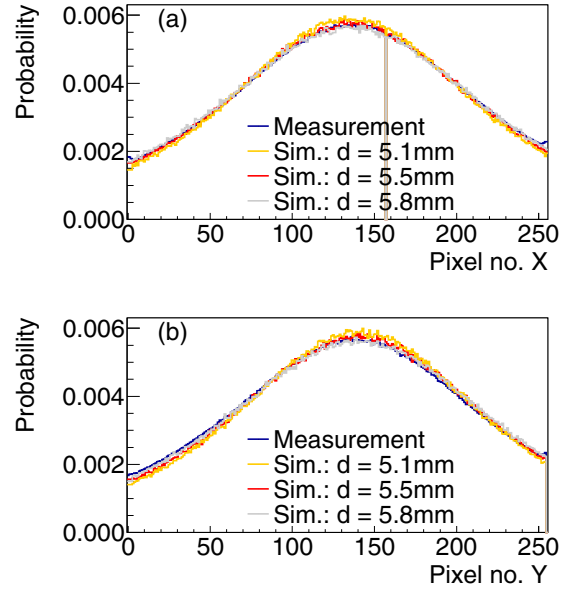

FIG. 3. (Color online) Detector B: Measured and simulated distributions of the points of detection (a) projected to the x axis (detector rows) in Fig. 1, and (b) projected to the y axis (detector columns) in Fig. 1. The simulations (Sim.) were carried out for different distances d between the source and detector B.

with f_{fine}) or 1145 μs (measurements with f_{coarse}) and initiated the readout of the detectors. Coincident frames could be acquired continuously over long time periods with a frame repetition rate of up to 48 Hz. The dead time, caused by the readout of the detectors and the data acquisition, relative to the live time amounted to 98.94% with f_{fine} and 94.5% with f_{coarse}. This large amount of dead time was due to the fact that in the frame-based readout scheme of the Timepix always the complete pixel matrix had to be read out although the occupancy of the average frame was only 1.3 (f_{fine}) or 6.5 (f_{coarse}). This limitation will be overcome with the next generation pixel detector Timepix3 [30] which has an event driven readout architecture.

The discriminator threshold is provided to all pixels by one digital-analog converter. The digital-analog converter is controlled by a register in the periphery of the ASIC. Each register value i had to be calibrated to energy $E(i)$. A threshold calibration was performed acquiring fixed frame-length photon counting images with each possible register value i under illumination of the detector with diagram line fluorescence photons (Mn K, Pb L, Sn K lines) generated by illuminating various foils with x rays from an x-ray tube. For each value i of the register, the total number of hits on the pixel matrix $N(i)$ was determined. The histogram $\Delta N(i) \equiv N(i+1) - N(i)$ reveals peaks which are due to photoelectric absorption in the silicon sensor with registration of almost the full energy deposited in the pixels. It has to be pointed out that the positions of the peaks do not correspond to the energies of the fluorescence photons but are shifted slightly to lower energy depositions, because of charge-sharing effects. Charge sharing between neighboring pixels, which reduces the detection efficiency and worsens energy resolution, is due to the extended track length of photoelectrons or Compton electrons and due to the lateral diffusion of holes during their drift to the pixel electrodes. The threshold was therefore calibrated with respect to deposited energy. The energy deposition spectrum for irradiation with the said fluorescence lines was simulated with a Monte Carlo simulation (described in Sec. II B) and the peak positions were determined. These positions served as ordinate of the discriminator threshold calibration curve $E(i)$ which reflects the correlation between measured peak position given in register steps and the simulated deposited energy. Register gains of (88.96 ± 0.17) eV/register step for detector A and (90.03 ± 0.26) eV/register step for detector B were obtained. The thresholds for the measurement were set as low as possible to (3.15 ± 0.10) keV (detector A) and (3.26 ± 0.33) keV (detector B) in order to achieve maximum efficiency for the fluorescence photons. With these settings, manganese fluorescence photons were not able to trigger more than two pixels.

In detector B, one column had a digital defect and could not be read out. This column was therefore omitted in the data analysis and in the simulation.

A mechanical support structure for source and x-ray detectors was built. The distance between the common electrode of each sensor to the center of the source was $\approx$5 mm. Good accuracy in the determination of source-detector distances and the lateral positions (x and y directions in Fig. 1) of the two detectors was obtained by matching the simulated spatial distribution of detected K-diagram line photons with the corresponding measured distribution. The measured distribution of hits in the detectors could be reproduced by the simulation with distances of (5.1 ± 0.1) mm for detector A and (5.5 ± 0.2) mm for detector B. In Figs. 2 and 3, the simulated

and measured distributions projected to the column and to the row axis are compared for the two detectors. Excellent agreement was achieved.

Electrons can also be ejected from the L or higher shells after K-shell electron captures or from the K shell after L- or even higher-shell electron captures. These processes do not give rise to two K-shell vacancies but also can result in two detectable particles (x ray and electron) emerging from the source. In order to keep systematic uncertainties of P_{KK} as small as possible, the detection yield for shake-off electrons was minimized by inserting Kapton foils (labeled 3A and 3B in Fig. 1) between the radioactive source and the x-ray detectors. The thickness was chosen so that as many electrons as possible were absorbed with still acceptable losses in the detection yield for hypersatellite and satellite photons. The thickness of the Kapton foils was derived from the area, weight, and density of $\rho = (1.4200 \pm 0.0007)$ g/cm^3. A thickness of (50.7 ± 1.4) μm was obtained.

The radioactive source used in the presented study had an activity of $A_0 = (72.5 \pm 1.1)$ kBq at 0:00 CET on August 1, 2011, certified by the German national metrology institute PTB. It comprised an aluminum ring with 30 mm outer and 20 mm inner diameter and 3 mm thickness in which two (23.40 ± 0.07) μm thick foils of polyethylene were spanned. Possible contaminations with ^{59}Fe (half life of 45 days) and ^{55}Co (half life of 17.53 h) were negligible after the long storage time of more than 12 years between the production of the ^{55}Fe and the measurements. Gamma spectrometry, carried out at the German metrology institute PTB, confirmed that no such contaminants were present. In the production of the source by the PTB, 20 mg of iron ions were dissolved in 1-l diluted aqueous solution of HCl with a concentration of 0.1 mol per liter. 12.62 mg of this solution was deposited as a circular spot with approximately 2.5 mm diameter and dried on top of one of the polyethylene foils. After drying, the source was sealed with the second thin polyethylene foil.

B. Detector simulation

In the following, the detection efficiency ϵ shall describe the probability that a particle, emitted from the source and hitting the sensor, is indeed detected in one or two neighboring pixels of the detector. The detection yield $\delta = \eta \times \epsilon$ for a specific particle type was defined as the product of the detection efficiency ϵ for this particle multiplied by the probability η that such an emitted particle reaches the detector sensitive volume. The detection yield δ represents the probability that a particle that is emitted in the source reaches the detector and is detected there in one or two neighboring pixels. A set of adjacent triggered pixels is referred to as one cluster.

A Monte Carlo simulation of the experiment was carried out in order to determine the detection yields for K-shell shake-off electrons after K capture and the influence of background events such as internal bremsstrahlung, K-, L-, and M-shell electron ejection. The simulation has been performed with the Monte Carlo package ROSI [31] based on EGS4 combined with the low energy extension LSCAT. The simulation setup of the experiment comprised the radioactive ^{55}Fe distribution, support polyethylene foils, aluminum ring, the two additional Kapton foils between source and detectors, silicon sensor layer ($14 \times 14 \times 0.3$ mm^3), under-bump metallization, bump bonds, under-bump metallization on the ASIC side, the silicon readout ASIC Timepix, ground connection plate of the ASIC, and FR4 readout board. For each ionizing particle, the number of collected holes was determined for every pixel in the pixel matrix. During processing of each event, the stepwise energy deposition of the electron (photoelectron or Compton electron, K-, L-, M-shell shake-off electron) in each segment along the trajectory in the silicon sensor was converted to an equivalent number of released electron-hole pairs. On average, 3.6 eV energy loss of the ionizing particle is necessary to create an electron-hole pair in silicon. The electron-hole pairs were distributed equally spaced in each segment of the trajectory. Each released hole was transported individually to the pixel electrode plane. Charge carrier diffusion was taken into account by randomizing the position of collection of the hole with a Gaussian distribution with a standard deviation calculated with the model of Spieler and Haller [32]. The spectra of deposited energies in the Timepix detector, including the tails to lower energies caused by charg -sharing, could be reproduced with this simulation with high accuracy, as it was previously demonstrated by Sievers *et al*. [33].

The noise in the analog output of the amplifier and the mismatch of discriminator threshold levels in the pixel matrix were taken into account by adding a random noise contribution to the number of collected holes. This noise contribution was obtained with a random number generator based on a Gaussian probability distribution with a standard deviation of 110 electrons. The number of collected holes was then converted to an equivalent deposited energy in each pixel. This energy deposition was compared to the discriminator threshold known from energy threshold calibration in each pixel. If the deposited energy was larger than threshold, a hit was assigned to the pixel.

C. Measurement principle: The signal

For double K-shell vacancy creation in K-shell electron capture, the particles that could in principle be detected with our setup are $K\alpha^H$ and $K\beta^H$ hypersatellite photons with energies [6] of (6.16 ± 0.02) keV and (6.835 ± 0.035) keV, the $K\alpha L^1$ and $K\beta L^1$ satellite photons with energies [34] of (5.933 ± 0.003) keV and (6.586 ± 0.003) keV, and the ejected K-shell electron with a broad energy distribution. An endpoint energy of about 218 keV is expected from theory [35] for the K-shell shake-off electrons. Low energy Auger electrons are stopped in the source material, the polyethylene foils, or in the additional Kapton foils. Therefore, they can not be detected.

In the following, the subscripts KK, KL, LK are assigned to quantities concerning electron ejection and specify the shell of the captured electron followed by the shell where a second vacancy is created by electron ejection. For example, LK stands for L capture followed by the shake-off of a K-shell electron. A is the electron capture rate in the ^{55}Fe source. T means the overall measuring time. τ denotes the relative live time of the data acquisition, $(1 - \tau)$ is the dead time relative to the overall measuring time. P_K is the ratio of the number of K-shell electron captures to the number of electron captures.

ω_K is the K-shell fluorescence yield of manganese. To the best of our knowledge, no measurements exist for the fluorescence yields of K-shell vacancy filling in presence of an additional vacancy. In all previous measurements of P_{KK} in literature, it was assumed that an additional vacancy does not affect the fluorescence yield in K-vacancy filling. Therefore, we assumed that $\omega_K = \omega_S = \omega_H$. The subscript H assigned to quantities concerning photon emission refers to hypersatellite photons and S refers to satellite photons of the manganese daughter atom.

Five combinations of detected particle pairs in the set of hypersatellite, satellite, and ejected electron were considered as signatures for double K-shell vacancy production.

The dominant combination in our experiment was the coincident detection of the hypersatellite and the satellite photon after K-shell capture, whereas the K-shell shake-off electron was not detected or the number of pixels triggered by the electron was larger than 2. The number N_1 of these events recorded by the apparatus and passing data analysis could be written as

$$N_1 = A\ P_K\ \tau\ T\ P_{KK}\ \delta_H\ \delta_S\ \omega_K^2\ (1 - \delta_{KK}). \quad (1)$$

$(1 - \delta_{KK})$ reflects that the K-shell shake-off electron was not detected. It was either absorbed in the source or foil, was scattered away on its flight to the detector, or it triggered no pixel or more than 2 pixels. The detection yield δ_{KK} for K-shell shake-off electrons after K capture was determined with the Monte Carlo simulation. In the simulation, electrons were emitted isotropically in the radioactive source with the energy spectrum presented by Chon and Law [36]. We obtained $\delta_{KK} = 1.52^{+0.13}_{-0.08} \times 10^{-3}$.

The second combination was the detection of the satellite photon together with the K-shell shake-off electron, whereas the hypersatellite photon was generated but not detected:

$$N_2 = A\ P_K\ \tau\ T\ P_{KK}\ (1 - \delta_H)\ \delta_S\ \omega_K^2\ \delta_{KK}. \quad (2)$$

With the values given in Table I, N_2 amounted to about 0.36 % of N_1.

The third combination was the detection of the hypersatellite photon together with the K-shell shake-off electron, whereas the satellite photon was emitted but not detected:

$$N_3 = A\ P_K\ \tau\ T\ P_{KK}\ \delta_H\ (1 - \delta_S)\ \omega_K^2\ \delta_{KK}. \quad (3)$$

With the values given in Table I, one calculates that N_3 amounted to about 0.38 % of N_1.

The fourth combination was the detection of the hypersatellite photon together with the K-shell shake-off electron, whereas the filling of the second K-shell vacancy does not lead to satellite photon emission, but to Auger electron emission, which could not be detected:

$$N_4 = A\ P_K\ \tau\ T\ P_{KK}\ \delta_H\ \omega_K\ (1 - \omega_K)\ \delta_{KK}. \quad (4)$$

With the values given in Table I, one derives that N_4 amounted to 1.12 % of N_1.

The fifth combination was the detection of the satellite photon together with the K-shell shake-off electron, whereas the filling of the first vacancy did not lead to a hypersatellite line photon but to Auger electron emission:

$$N_5 = A\ P_K\ \tau\ T\ P_{KK}\ \delta_S\ (1 - \omega_K)\ \omega_K\ \delta_{KK}. \quad (5)$$

TABLE I. Simulated, measured, and calculated values of parameters of this experiment with their statistical (1σ) and systematic uncertainties $(\Delta x)_{\text{syst}}$.

Quantity x	Value	$\sigma(x)$	$(\Delta x)_{\text{syst}}$
κ_H	1.0499	0.0008	$^{+0.0048}_{-0.0062}$
κ_S	1.0118	0.0008	$^{+0.0013}_{-0.0031}$
δ_K^{fine}	2.8585×10^{-1}	1.5×10^{-5}	± 0.0044
δ_K^{coarse}	2.8450×10^{-1}	1.0×10^{-5}	± 0.0044
δ_{IB1S}	0.01689		± 0.0011
δ_{KK}	1.52×10^{-3}		$^{+0.13}_{-0.08} \times 10^{-3}$
$\delta_{KL,LK}$	3.12×10^{-4}		$^{+0.59}_{-0.06} \times 10^{-4}$
γ_{SH}	0.997	0.0014	
γ_{Se}	0.992	0.0200	
γ_{He}	0.996	0.0200	
$P_{\text{loss}}^{\text{fine}}$	0.106	0.003	
$P_{\text{loss}}^{\text{coarse}}$	0.087	0.002	
A_0 [kBq]	72.5		± 1.1
$N_{\text{prompt}}^{\text{fine}}$ - $N_{\text{acc}}^{\text{fine}}$	5703	437	
$N_{\text{prompt}}^{\text{coarse}}$ - $N_{\text{acc}}^{\text{coarse}}$	10726	693	
$\dot{N}_{\text{bg,ext}}$ [s^{-1}]	6.47×10^{-4}	0.61×10^{-4}	
N_K^{coarse}	7.4827×10^8	2.7×10^4	
N_K^{fine}	3.5860×10^8	1.9×10^4	
$T(f_{\text{coarse}})$ [d]	50.6		
$T(f_{\text{fine}})$ [d]	27.9		
$T_{\text{mock}}(f_{\text{coarse}})$ [d]	27.3		
$\tau(f_{\text{coarse}})$	0.0742		
$\tau(f_{\text{fine}})$	0.0175		
$\tau_{\text{mock}}(f_{\text{coarse}})$	0.0742		

With the values given in Table I, one can see that N_5 amounted to 1.08 % of N_1.

The K-shell shake-off electron detection yield δ_{KK} was obtained by simulating isotropically emitted electrons with the spectrum given in Ref. [36]. The number of electrons which triggered one or two adjacent pixels in one cluster was determined per emitted electron. In the data analysis of the P_{KK} measurement, only events that triggered exactly two clusters, with one or two adjacent triggered pixels each, were regarded as signal events. We obtained $\delta_{KK} = 1.52 \times 10^{-3}$. This indicates that 99.85 % of the K-shell shake-off electrons lost too much energy in the source or the foil to trigger the detector, were scattered away or generated a track in the detector with more than two adjacent triggered pixels.

A significant amount of prompt background, originating from other sources than ^{55}Fe, could be reduced by rejecting events in the data analysis with two clusters on one detector that had a distance smaller than 10 pixels (0.55 mm) to each other (see Sec. II F). A simulation was carried out in order to determine the reduction of solid angle acceptance caused by this cut. N_{pairs} particle pairs (satellite and hypersatellite photon, satellite photon and K-shell shake-off electron, hypersatellite photon and K-shell shake-off electron) were emitted from the source into the complete solid angle. The number of events $N_{\text{pairs, det}}$ passing the cut on the cluster separation distance was determined. The relative solid angle acceptance was

calculated as $\gamma_{\mathrm{P1P2}} \equiv N_{\mathrm{pairs,\,det}}/N_{\mathrm{pairs}}$ for each combination of the particles P1 and P2.

In total, the number of signal events was given by

$$\begin{aligned} N_{\mathrm{Signal}} = A\ P_K\ \tau\ T\ P_{KK}\big[&\delta_H\ \delta_S\ \omega_K^2\ (1-\delta_{KK})\ \gamma_{SH} \\ &+(1-\delta_H)\ \delta_S\ \omega_K^2\ \delta_{KK}\ \gamma_{\mathrm{Se}} \\ &+\delta_H\ (1-\delta_S)\ \omega_K^2\ \delta_{KK}\ \gamma_{\mathrm{He}} \\ &+\delta_H\ \omega_K\ (1-\omega_K)\ \delta_{KK}\ \gamma_{\mathrm{He}} \\ &+\delta_S\ (1-\omega_K)\ \omega_K\ \delta_{KK}\ \gamma_{\mathrm{Se}}\big]. \end{aligned} \tag{6}$$

The number of recorded diagram line photons after single vacancy producing K-shell electron captures could be expressed as

$$N_K = A\ P_K\ \tau\ T\ \delta_K\ \omega_K. \tag{7}$$

Combining Eqs. (6) and (7) gave

$$\begin{aligned} N_{\mathrm{Signal}} = P_{KK} N_K[&\kappa_H\ \kappa_S\ \delta_K\ \omega_K\ (1-\delta_{KK})\ \gamma_{\mathrm{SH}} \\ &+\kappa_S\ (1-\kappa_H\ \delta_K)\ \omega_K\ \delta_{KK}\ \gamma_{\mathrm{Se}} \\ &+\kappa_H\ (1-\kappa_S\ \delta_K)\ \omega_K\ \delta_{KK}\ \gamma_{\mathrm{He}} \\ &+\kappa_H\ (1-\omega_K)\ \delta_{KK}\ \gamma_{\mathrm{He}} \\ &+\kappa_S\ (1-\omega_K)\ \delta_{KK}\ \gamma_{\mathrm{Se}}], \end{aligned} \tag{8}$$

with $\kappa_H \equiv \delta_H/\delta_K$, $\kappa_S \equiv \delta_S/\delta_K$. $\kappa_H = 1.0499 \pm 0.0008$ and $\kappa_S = 1.0118 \pm 0.0008$ could be determined with the Monte Carlo simulation. The quantities κ were introduced because they were independent from the specific geometry of the setup and less sensitive to threshold variations than δ_H and δ_S. The systematic error on κ given in Table I results from uncertainties in the discriminator thresholds. δ_K was determined from the measured number of detected diagram line photons N_K with negligible statistical error as

$$\delta_K = \frac{N_K}{N_{ec}\ P_K\ \omega_K}. \tag{9}$$

Here, N_{ec} is the number of electron-capture decays during the lifetime of the measurement. $N_{ec} = \sum_i N_{ec,i}$ is calculated from the number of electron-capture decays $N_{ec,i}$ during the lifetimes of all runs i. The number of decays during each run i is calculated by

$$N_{ec,i} = A_0\ \tau\ \Delta T_i\ 2^{-\frac{\Delta t_i}{T_{1/2}}}, \tag{10}$$

where Δt_i is the time elapsed after calibration measurement of the source activity and the middle of the run, and ΔT_i is the duration of the run.

Table I gives the values of quantities characterizing the experimental setup and the measurement. It shall be pointed out that the simulated diagram line photon detection yield of $\delta_K = 0.3083^{+0.027}_{-0.028}$ agreed with the measured values given in Table I.

D. Measurement principle: The background

Now, the background processes which could influence the measurement of P_{KK} are discussed. It will be explained how these contributions could be eliminated in the calculation of P_{KK}.

The processes which could mimic a signal event in the experiment and analysis could be grouped into ^{55}Fe-decay-related accidental coincidences N_{acc}, ^{55}Fe-decay-related prompt background $N_{\mathrm{bg,Fe55}}$ due to shake-off electrons and internal bremsstrahlung, and non-^{55}Fe-decay-related background $N_{\mathrm{bg,ext}}$ like natural background. One could write

$$N_{\mathrm{Signal}} = (N_{\mathrm{prompt}} - N_{\mathrm{acc}}) - N_{\mathrm{bg,Fe55}} - N_{\mathrm{bg,ext}}, \tag{11}$$

where N_{prompt} was the number of events with two clusters of pixels triggered in the coincidence window which was defined in the data analysis. $(N_{\mathrm{prompt}} - N_{\mathrm{acc}})$ was corrected for a loss of signal events caused by accidental vetoes of signal events by random coincidences with a detected diagram line photon in the data analysis procedure. This correction will be explained in more detail in Sec. II F.

The dominant source of background related to the electron-capture decay itself was the accidental detection of two K-diagram line fluorescence photons of ^{55}Mn in coincidence in one detector (two clusters in one detector) or in two detectors (one cluster in each detector). The number of random coincidences N_{acc} was determined similar to the delayed coincidence technique from the measured time spectra.

Another source for decay-related background was the ejection and detection of L shake-off electrons after K-electron capture with simultaneous detection of the K-diagram line photon. The L-fluorescence photon could not be detected because its energy was below discriminator threshold. An additional decay-related background was the ejection and detection of a K-shell shake-off electron and the emission and detection of a satellite line photon after L-electron capture. Primakoff and Porter [19] developed a theoretical description of electron ejection in electron-capture decays. Pengra and Crasemann [35] carried out the first and, to the best of our knowledge, only measurement of the energy spectrum of atomic electrons ejected in the electron-capture decay of ^{55}Fe. It was found that the slope of the measured electron energy spectrum in coincidence with K-diagram line photons (K capture and L shake-off plus L capture and K shake-off) differs from the theoretical expectation based on the theory of Primakoff and Porter, especially for electron energies below approximately 70 keV and above approximately 140 keV. Pengra and Crasemann stated that the contribution of L-shake-off electrons after K capture relative to K shake-off after K capture is in the order of 10^{-3} for the observed electron energies which were between approximately 20 and 200 keV. For the calculation of the L-shell contribution, they followed Wolfsberg's suggestion [37] and modified Levinger's [38] theory of L-electron excitation in ordinary beta decay [where $(\Delta Z_{\mathrm{eff}})^2 = 1$] by correcting for the reduced effect of the change of the nuclear charge on L electrons in electron captures (due to screening by the K-shell electron). Their result was $(\Delta Z_{\mathrm{eff}})^2 = 0.0225$ for electron-capture decays using Slater's [39] recipe for estimating shielding effects. Figure 8 in the work of Pengra and Crasemann shows that the contribution of L electrons to the total amount of electrons emitted after electron capture in ^{55}Fe would be only of importance for low electron energies below 30 keV. This can be also seen in the work of Chon and Law [36]. In Fig. 1 of their work, the

electron spectra for K-capture L shake-off (KL) combined with L-capture K shake-off (LK) are compared to the electron energy spectra for K-capture K shake-off after K capture (KK). Due to the additional Kapton foil between source and detectors, electrons with energies smaller than 70 keV have detection yields of less than $(2.64 \pm 0.76) \times 10^{-4}$ calculated from simulation results. Thus, the influence of electron emissions involving the L shell was strongly suppressed in our experiment.

The contribution of the two background processes K shake-off after L capture and L shake-off after K capture, both with detection of the ejected electron and the satellite photon, could be modeled similarly to the signal contributions [see Eqs. (1)–(5)] as

$$\begin{aligned} N_{KL,LK} &= A\ P_K\ \tau\ T\ P_{KL,LK}\ \omega_K\ \delta_S\ \delta_{KL,LK} \\ &= N_K\ P_{KL,LK}\ \kappa_S\ \delta_{KL,LK}, \end{aligned} \tag{12}$$

where $P_{KL,LK} = 3.161 \times 10^{-4}$ was the probability of electron ejection from K/L shell in L-/K-electron captures over the full electron energy range relative to K capture calculated by Chon and Law [36]. A simulation of the combined detection yield $\delta_{KL,LK}$ for K-shell shake-off electrons after L capture and L-shell shake-off electrons from K capture emitted isotropically in the radioactive source with the energy spectrum presented in [36] resulted in $\delta_{KL,LK} = 3.12^{+0.59}_{-0.06} \times 10^{-4}$. Therefore, K-/L-shell electron emission after L-/K-electron capture ($N_{KL,LK}$) contributes only with 0.8% of N_1 to the number of detected events if one assumes $P_{KK} = (1.3 \pm 0.2) \times 10^{-4}$ measured by Campbell *et al.* [2]. Nevertheless, this source of background was taken into account.

M-shell shake-off following K-electron capture was an additional source of background which could mimic a double-K-shell vacancy production. The M-shell shake-off electron might have been detected in coincidence with a fluorescence photon from the single K-shell vacancy filling after K-electron capture. Mukoyama [40] calculated M-subshell shake-off probabilities per K-electron capture and obtained for the processes involving different M subshells: $P_{KM_1} = 0.254 \times 10^{-4}$, $P_{KM_2} = 2.64 \times 10^{-4}$, $P_{KM_3} = 4.08 \times 10^{-4}$, $P_{KM_4} = 1.33 \times 10^{-4}$, $P_{KM_5} = 0.481 \times 10^{-4}$. This resulted in a total probability for M-shell shake-off after K capture of $P_{KM} = 8.722 \times 10^{-4}$. The energy spectra of M-shell electrons ejected in K capture presented by Mukoyama [40] are much softer than the energy spectra of L-shell electrons [36] ejected in K capture. Although P_{KM} is larger than P_{KL}, the influence of M-shell electrons on the measurement was much smaller in our experiment because a significant yield was only present for energies above 70 keV. To the best of our knowledge, neither calculations nor measurements of the energy spectra of M-shell shake-off electrons following K capture in ^{55}Fe were performed up to now for energies above 30 keV. Therefore, an upper limit for the detection probability of an M-shell shake-off following K capture was estimated. Let us assume that the probability density $\tilde{P}(E)$ that an electron ejected from an M subshell with energy E does not decrease further for energies larger than 30 keV. It shall then equal the smallest value that was predicted for the probability density per subshell electron and per K capture (Fig. 1 in [40]) for energies below 30 keV. The limits of the probability densities extracted from Mukoyama's analysis [40] are $\tilde{P}_{M1,3,4,5}(30\ \text{keV}) = 6 \times 10^{-8}\ [1/m_e c^2]$ for M_1, M_3, M_4, M_5, and $\tilde{P}_{M2}(30\ \text{keV}) = 1 \times 10^{-7}\ [1/m_e c^2]$ for M_2. Taking into account the individual population of the M subshells, one obtains a maximum probability of $P^{\max}_{KM} = 3.75 \times 10^{-7}$ per K capture that a M electron is ejected in K capture with an energy between 30 and 231 keV. The simulated average detection yield for M-shell shake-off electrons then amounted to $\overline{\delta_{KM}} = 0.069$. The maximum number of events with detection of an M-shell shake-off electron after K capture together with the corresponding fluorescence photon was $N^{\max}_{KM} = A\ P_K\ \tau\ T\ P^{\max}_{KM}\ \delta_K\ \omega_K\ \overline{\delta_{KM}}$. This contribution was only about 0.2% of the number of detected events with satellite and hypersatellite photons in coincidence (N_1). The M-shell shake-off contribution was neglected in our analysis because the M-shell electron ejection probability decreases further with electron energy for energies larger than 30 keV as it also does for K and L shake-off electrons.

M-shell electron capture followed by K-shell electron shake-off is suppressed by a factor $P_M/P_K = 0.017$. Thus, an even smaller influence of M capture followed by K-shell electron shake-off to the signal was expected compared to K capture followed by M shake-off. Therefore, this contribution was also neglected. The contribution of ejection of N-shell electrons was even smaller than the contribution of ejection from the M shell because of the smaller number of available electrons, even smaller ejection energies, and the smaller N-shell electron-capture rate compared to the M shell. The N-shell contribution could therefore also be neglected.

An additional source of decay-related background was the detection of an internal bremsstrahlung photon emitted by the captured K-shell electron in coincidence with the detection of the diagram line K-fluorescence photon of ^{55}Mn. Internal bremsstrahlung photons obey a broad energy spectrum [23] up to a maximum energy of 231.21 keV. The internal bremsstrahlung photons following K capture mostly have energies above discriminator thresholds and could trigger pixels, while the emitted diagram line fluorescence photon could trigger a second cluster so that the signature was similar to the detection of satellite and hypersatellite photons following K capture. For ^{55}Fe the internal bremsstrahlung emission probability is $P_{\text{IB}} = 3.24(6) \times 10^{-5}$ per K-shell electron capture in the photon energy range between 35 and 231 keV [41]. It has to be pointed out that this value is stated as total internal bremsstrahlung probability in Ref. [23]. It is the same value given in the earlier, original work of Isaac *et al.* [41], but explained there as measured P_{IB} for photon energies between 35 and 231 keV. Therefore, one can assume that the value given in Ref. [23] is not correctly reflecting the total bremsstrahlung production probability. For a proper subtraction, the probability density for bremsstrahlung emission measured by Isaac *et al.* had to be extrapolated to the broader energy range of the pixel detectors used in this work. A numerical integration of the probability density for internal bremsstrahlung production after captures from the different subshells given in Fig. 3 of Ref. [41] was carried out. The

total probability P_{IB} measured by Isaac *et al.* [41] was then decomposed into the contributions for captures from various shells. The internal bremsstrahlung production probability in K-shell electron capture in the energy range from 35 to 231 keV was calculated. The result was $P_{\mathrm{IB1S}}(E > 35\ \mathrm{keV}) = 2.4233 \times 10^{-5}$. The internal bremsstrahlung production probability in K-electron capture for photon energies smaller than 35 keV was calculated by integrating the probability density as a function of photon energy for $1S$ capture given in Fig. 1 of Biavati *et al.* [42] in the low photon energy range. The calculation of Biavati *et al.* [42] is based on the prediction of Martin and Glauber [43] with screening correction and relativistic kinematics taken into account. In total, a probability of internal bremsstrahlung production in the energy range from 3 to 231 keV of $P_{\mathrm{IB1S}} = 1.065 \times P_{\mathrm{IB1S}}(E > 35\ \mathrm{keV}) = 2.5808 \times 10^{-5}$ (per K-electron capture) was obtained. A Monte Carlo simulation using the photon energy spectrum given in Biavati *et al.* [42] for $1S$-electron capture in the full energy range revealed a detection yield of internal bremsstrahlung photons in our experiment of $\delta_{\mathrm{IB1S}} = (1.69 \pm 0.11)\%$. The number of background events caused by internal bremsstrahlung was taken into account with

$$\begin{aligned} N_{\mathrm{IB}} &= A\ P_K\ \tau\ T\ \delta_K\ \omega_K\ P_{\mathrm{IB1S}}\ \delta_{\mathrm{IB1S}} \\ &= N_K\ P_{\mathrm{IB1S}}\ \delta_{\mathrm{IB1S}}. \end{aligned} \tag{13}$$

Internal bremsstrahlung contributes with 3.5% of N_1 to the number of detected signal events if one assumes $P_{KK} = (1.3 \pm 0.2) \times 10^{-4}$ measured by Campbell *et al.* [2].

For the decay-related background, one obtains

$$\begin{aligned} N_{\mathrm{bg,Fe55}} &= N_{\mathrm{IB}} + N_{KL,LK} \\ &= N_K\ (P_{\mathrm{IB1S}}\ \delta_{\mathrm{IB1S}} + P_{KL,LK}\ \kappa_S\ \delta_{KL,LK}). \end{aligned} \tag{14}$$

A measurement with a mock of the radioactive source in the same setup was performed in order to eliminate contributions to the signal caused by natural radioactivity in the environment, cosmic rays, and caused by radioactive contaminants in the detectors, readout electronics, cables, Kapton foils, support structure, aluminum ring, and dried carrier solvent for ^{55}Fe. This mock was identical to the used radioactive source except that it did not contain the ^{55}Fe itself. The number of expected external background events $N_{\mathrm{bg,ext}} = \dot{N}_{\mathrm{bg,ext}} \tau T$ to the measurement of P_{KK} was $(1.44 \pm 0.14)\%$ of the number of detected signal events. This contribution is subtracted from the measurement with the radioactive source.

E. Calculation of P_{KK}

Finally, the number of signal events to be determined from measured data is given by

$$\begin{aligned} N_{\mathrm{Signal}} &= (N_{\mathrm{prompt}} - N_{\mathrm{acc}}) - N_{\mathrm{bg,Fe55}} - N_{\mathrm{bg,ext}} \\ &= (N_{\mathrm{prompt}} - N_{\mathrm{acc}} - N_{\mathrm{bg,ext}}) - N_K \\ &\quad \times (P_{\mathrm{IB1S}}\ \delta_{\mathrm{IB1S}} + P_{KL,LK}\ \kappa_S\ \delta_{KL,LK}). \end{aligned} \tag{15}$$

With Eq. (8) one finds that the double-vacancy creation probability per K-shell electron capture P_{KK} could be determined via

$$P_{KK} = \frac{\frac{N_{\mathrm{prompt}} - N_{\mathrm{acc}}}{1 - P_{\mathrm{loss}}} - N_{\mathrm{bg,ext}} - N_K \times (P_{\mathrm{IB1S}}\ \delta_{\mathrm{IB1S}}\ \gamma_{\mathrm{IB1S,K}} + P_{KL,LK}\ \kappa_S\ \delta_{KL,LK}\ \gamma_{\mathrm{Se}})}{N_K\ \omega_K \left[\gamma_{SH}\ \kappa_H\ \kappa_S\ \delta_K (1 - \delta_{KK}) + \gamma_{\mathrm{Se}}\ \delta_{KK}\ \kappa_S \left(\frac{1}{\omega_K} - \kappa_H\ \delta_K\right) + \gamma_{\mathrm{He}}\ \delta_{KK}\ \kappa_H \left(\frac{1}{\omega_K} - \kappa_S\ \delta_K\right)\right]}, \tag{16}$$

where P_{loss} corrects for signal event losses during the data analysis by random vetoes due to diagram line photons. The reason for this correction was that time slices with more than two clusters triggered during the subframe were omitted during data analysis. Therefore, random vetoes could occur if a signal event is detected in a subframe, but a third cluster of triggered pixels due to a diagram line photon was present in the same time slice. This correction is described in detail in Sec. II F.

It has to be pointed out that the denominator in Eq. (16) in fact did not depend on ω_K because δ_K was determined with Eq. (9) from the measured number of diagram line photons as $\delta_K = N_K/(N_{ec} P_K \omega_K)$, where N_{ec} is the number of electron-capture decays during the lifetime of the measurement. Therefore, the measured P_{KK} does not depend on ω_K. This was important because x-ray photons with energies close to the diagram line photon energies are produced in the radiative Auger effect (RAE) [34]. Their intensity is about 0.5% of $K\alpha$ and 2.4% of $K\beta$ [2]. The radiative Auger effect manifests a tail in the energy spectrum on the low energy side of the diagram lines. In the analysis of Campbell *et al.* [2], this led to an additional degree of freedom. The reason is that their experiment was based on the decomposition of the measured energy spectrum into the various fluorescence lines with contributions from the radiative Auger effect. Campbell *et al.* modeled the RAE x rays by low intensity lines at 5.8 and 6.4 keV. In our measurement, x rays from the radiative Auger effect can not influence the result in a significant way because the major fraction of the RAE photons has energies very close to the diagram line energies. The detection yield for these RAE photons is thus almost identical to the detection efficiency for diagram line photons. The radiative Auger effect could therefore in principle be taken into account by a slightly increased ω_K, but this would not change P_{KK} determined via Eq. (16). Thus, the radiative Auger x-ray emission has no influence on our result.

F. Data analysis

3.723×10^8 frames with f_{fine} and 1.718×10^8 frames with f_{coarse} with the source were recorded in time-of-detection mode. 1.693×10^8 frames were recorded with the mock of the source. The effective measuring times amounted to $\tau_{\mathrm{fine}} T_{\mathrm{fine}} = 76556.81$ s, $\tau_{\mathrm{coarse}} T_{\mathrm{coarse}} = 178939.64$ s with the source, and $\tau_{\mathrm{coarse}} T_{\mathrm{mock}} = 176383.81$ s with the mock. Data

taking was carried out in approximately 1.7 days long runs, containing 6.62×10^6 frames each. The activity of the source was considered to be constant during each run. The data acquisition stored the coordinates (column number x, row number y) and the time of detection with respect to the end of the frame for each event, frame, and each detector in a data file.

Particles which have triggered a pixel just before shutter opening might have been recorded with large values for the time of detection. Their time of detection then corresponds to the moment of shutter opening and not to the moment of interaction in the sensor. In order to avoid any influence of these early events and to avoid eventual variations on the length of the NIM electronics gate defining the common length of the frames of the two detectors, a cut on the maximum time-of-detection time was applied in the data analysis. Events with a time of detection of more than 11 090 clock cycles (f_{fine}) and 10 000 clock cycles (f_{coarse}) were rejected in the analysis. So, the length of the frame used in the analysis amounted to 231 μs for f_{fine} and 1.042 ms f_{coarse}. For each frame, the complete duration was then divided in 10 (f_{fine}) or 50 (f_{coarse}) equally long subframes with short duration in order to facilitate the analysis and to reduce ambiguities that arise for the assignment of the coincidence partnerships between clusters of triggered pixels in the original longer frames. For each frame, the triggered pixels were assigned to one of these 10 (f_{fine}) or 50 (f_{coarse}) equally long time slices according to their time-of-detection values.

Each subframe was then analyzed separately for coincidentally triggered pixels. Pixels which were in connection with masked pixels or with the edges of the pixel matrix were omitted from data analysis. The analysis program then identified clusters, i.e., groups of adjacent triggered pixels, in the subframes. Each cluster was represented by the pixel with the earliest response (largest time-of-detection value). This was supposed to be the pixel which collected most of the deposited energy. Because of time walk, its time-of-detection value represents the moment of detection more accurately than the time-of-detection value of a pixel suffering more severely from charge sharing. Only if exactly two separated clusters were found in one subframe, the event is considered for further analysis. Events with two clusters of triggered pixels on one detector with a distance of less than 10 pixels (0.55 mm) from each other were rejected in order to reduce the amount of prompt background events. With this cut, the relative loss of signal events amounted to only about $(3.0 \pm 1.4) \times 10^{-3}$ (determined with Monte Carlo simulation assuming uncorrelated satellite-hypersatellite emission directions) while the background not stemming from the ^{55}Fe was reduced by 37.3%. Figure 4 shows the measured distribution of distances between two coincident clusters in one detector (A or B) collected with the mock of the radioactive source. The most probable source for these background events, which triggered pixels which were close to each other, is Compton scattering of background photons in a first pixel, combined with detection of the Compton scattered photon in a second pixel. The reason for an increased number of such events at small distances is that the solid angle acceptance for detecting the Compton scattered photon decreases with increasing distance between the first and second triggered pixel because of the thin sensor. This effect was already investigated in an earlier work [44].

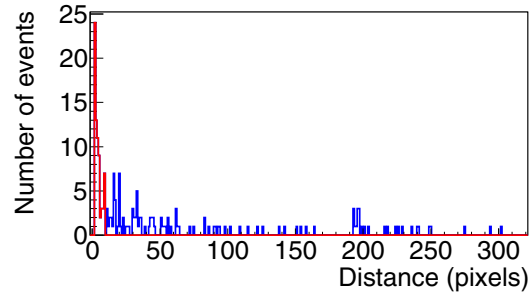

FIG. 4. (Color online) Distribution of distances between two coincident clusters in subframes in one of the detectors (A or B) measured with the mock of the radioactive source. Events (red) with a distance of smaller than 10 pixels were rejected in the analysis. The background was reduced by 37.3% with this cut.

After this cut, the difference in the time of detection of the two clusters was calculated. Figure 5 shows the spectrum of the time differences for the measurement with the clock frequency f_{fine}. The signal events appear as a tiny peak on a mountain of random coincidences. Figure 6 shows the corresponding time spectra for the measurement with f_{coarse}.

There was an artificial loss of signal events (two clusters of triggered pixels) in the data analysis due to the fact that signal events might have been vetoed in the analysis by an additional random coincidence with a diagram line photon in the subframe. The relative loss of signal events P_{loss} caused by this was determined with a numerical simulation of time-of-detection distributions. For each run, the actual activity was calculated. The average number of detected particles per frame was determined. A series of frames with time-of-detection time stamps was generated by randomizing mainly a uniform probability between 0 and the frame length, measured in clock cycles as in the experiment. Signal events (two clusters triggered in coincidence) were injected into the simulated train of time stamps. The time-of-detection difference between the two clusters was randomized with a Gaussian distribution (centered at 0 ns) with a standard deviation of 42 ns (73 ns) for f_{fine} (f_{coarse}) to mimic the influence of time walk. The number of injected signal events was determined using Eq. (8) with $P_{KK} = (1.3 \pm 0.2) \times 10^{-4}$ taken from the work of Campbell *et al.* [2] and randomized with the Poisson distribution. The average number of generated time stamps per frame equaled the average measured number of clusters per frame of the run. The exact value of P_{KK} has only negligible influence to the average number of clusters per frame. Thus, a synthetic series of frames was produced. Subframes were formed and coincidences in the subframes were counted. This simulation was repeated several times in order to take statistical fluctuations into account. The number of simulated signal events (coincidences) was determined. The relative loss of signal events P_{loss} due to cuts of the maximum acceptable time-of-detection value (edges), due to edges of the subframes and due to random vetoes was calculated. $P_{\text{loss}}^{\text{fine}} = 0.106 \pm 0.003$ and $P_{\text{loss}}^{\text{coarse}} = 0.087 \pm 0.002$ was obtained. Figures 7 and 8 show the measured and simulated time-of-detection

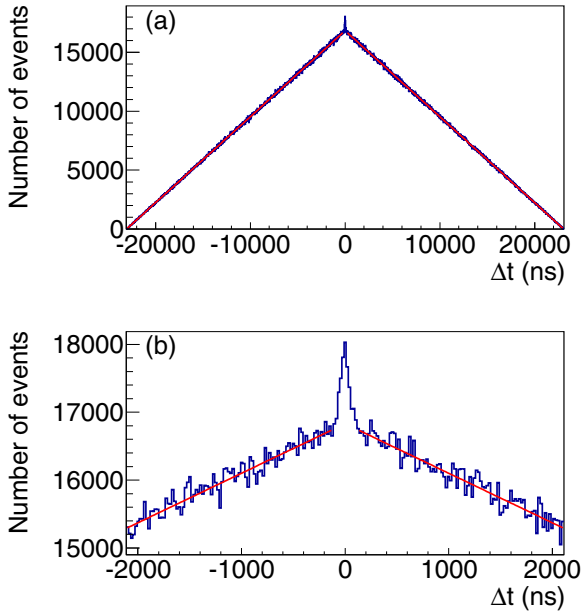

FIG. 5. (Color online) Distribution of the measured differences in the time-of-detection values of two clusters of triggered pixels for f_{fine} for the full range of accepted counter values in subframes (a) and in the prompt region (b). The result of the fit to the distribution of random coincidences is shown as straight, red line.

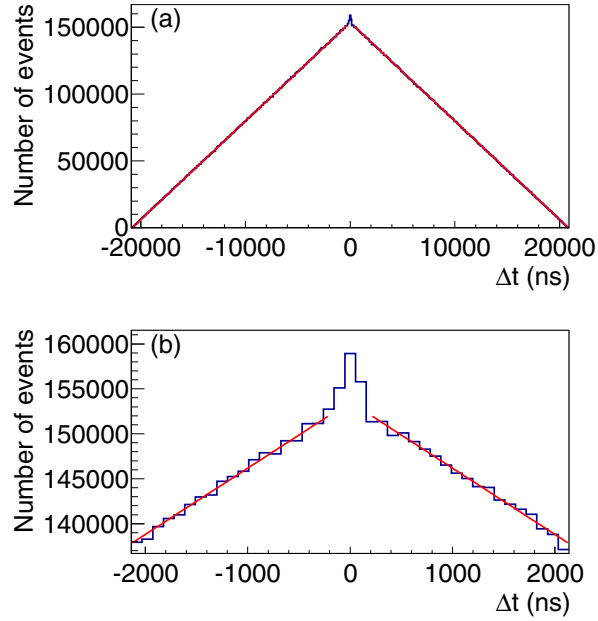

FIG. 6. (Color online) Distribution of the measured differences in time-of-detection values of two clusters of triggered pixels for f_{coarse} for the full range of accepted counter values in subframes (a) and in the prompt region (b). The result of the fit to the distribution of random coincidences is shown as straight, red line.

difference spectra in comparison to underline the accuracy of the simulated time stamps used for this correction.

To calculate P_{KK} from measured data, the numbers of events $N_{\text{prompt}}^{\text{fine}}$ and $N_{\text{prompt}}^{\text{coarse}}$ were determined by counting pairs of clusters (1 or 2 pixels triggered in each cluster) with absolute time differences smaller than 114.6 ns (156.3 ns) for f_{fine} (f_{coarse}). The probability that two independent diagram line photons, which were detected in a subframe of length t_{subframe}, were recorded with a time difference of Δt is given by $(t_{\text{subframe}} - \Delta t)/t_{\text{subframe}}$. This leads to the triangular shape $N_{\text{acc}}(\Delta t) = (a|\Delta t| + b)$ of the time-difference distribution of the random coincidences. This distribution can be seen in Figs. 5 and 6. A linear regression was carried out excluding the prompt region (time differences between -114.6 and 114.6 ns for f_{fine} and between -156.3 and 156.3 ns for f_{coarse}). We obtained $a_{\text{fine}} = (-0.7298 \pm 0.0002)$ ns^{-1}, $b_{\text{fine}} = 16831 \pm 4$ and $a_{\text{coarse}} = (-7.369 \pm 0.002)$ ns^{-1}, $b_{\text{coarse}} = 153544 \pm 30$. The number of random coincidences N_{acc} in the prompt region was calculated by summation of $N_{\text{acc}}(\Delta t)$ in the prompt peak region. The signal events were only approximately 3.1% (f_{fine}) and 2.3% (f_{coarse}) of the total number of detected events in the prompt region. This small signal-to-background ratio was a result of the long peaking time of the preamplifier output pulse, the time walk effect in combination with charge sharing in the sensor layer, and the small probability of double-vacancy production.

III. RESULTS AND DISCUSSION

The results of our measurement are $P_{KK} = (1.640 \pm 0.131) \times 10^{-4}$ for f_{fine}, $P_{KK} = (1.469 \pm 0.100) \times 10^{-4}$ for f_{coarse}, where the errors are the statistical uncertainties. The systematic errors are $(\Delta P_{KK})_{\text{syst}} = \pm 0.024 \times 10^{-4}$ for f_{fine} and $(\Delta P_{KK})_{\text{syst}} = \pm 0.022 \times 10^{-4}$ for f_{coarse}. The results of the two measurements with different clock frequencies agree within their statistical errors. For the whole campaign, we obtained a double-vacancy production probability and a statistical error of

$$P_{KK} = (1.531 \pm 0.079) \times 10^{-4}.$$

The systematic error was $(\Delta P_{KK})_{\text{syst}} = \pm 0.023 \times 10^{-4}$. This result is in agreement with $(1.3 \pm 0.2) \times 10^{-4}$ measured by Campbell *et al.* [2] within the stated uncertainties.

Now, the uncertainties in the measurement are discussed. N_{prompt}, N_{acc}, $N_{\text{bg,ext}}$, N_K vary according to Poissonian statistics. The error of N_K is negligible due to the large number of detected fluorescence photons (see Table I). Systematic inaccuracies arose from uncertainties in the source-detector distances, Kapton foil thickness, uncertainties in the discriminator thresholds, and the uncertainty in the source activity.

The discriminator thresholds could have affected the simulation results of κ_H, κ_S, δ_{KK}, $\delta_{KL,LK}$, δ_{IB}. Simulations of these quantities for discriminator thresholds shifted by the threshold uncertainties from energy calibration were carried out. The following bands were obtained for the relative systematic errors: $(\Delta\kappa_H)_{THL}/\kappa_H \in [-0.0059, 0.0046]$, $(\Delta\kappa_S)_{THL}/\kappa_S \in [-0.0030, 0.0012]$, $(\Delta\delta_{KK})_{THL}/\delta_{KK} \in [-0.004, 0.022]$, $(\Delta\delta_{KL,LK})_{THL}/\delta_{KL,LK} \in [-0.0096, 0.054]$, $(\Delta\delta_{\text{IB1S}})_{THL}/\delta_{\text{IB1S}} \in [-0.0056, 0.0039]$.

Errors in the source-detector distances could have affected the simulation results of δ_{KK}, $\delta_{KL,LK}$, δ_{IB}. The determination of δ_K was not affected by the source-detector distances because it was calculated via Eq. (9) from measured data. By

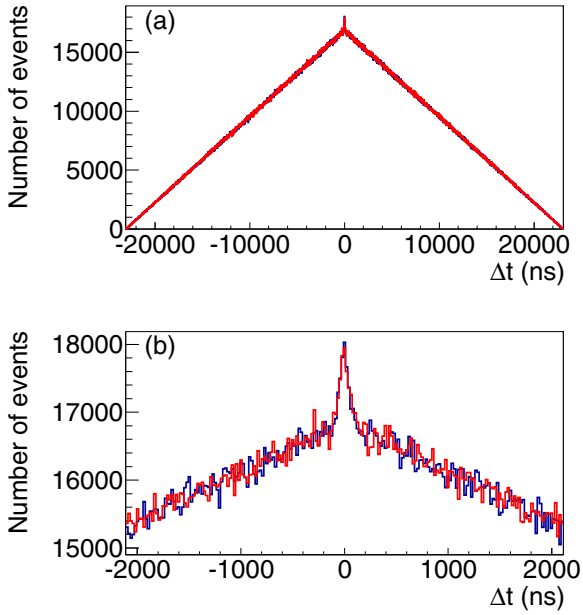

FIG. 7. (Color online) Simulated (red) and measured (blue) time-of-detection difference histograms for full length of the subframes (a) and close to the prompt region (b) for f_{fine}.

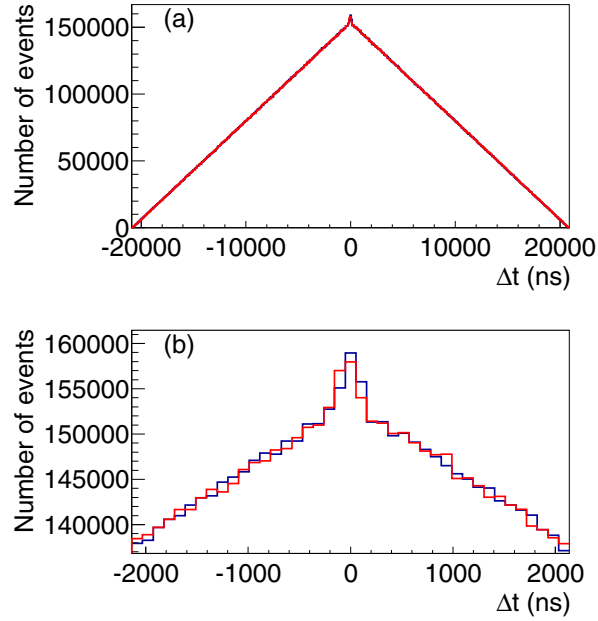

FIG. 8. (Color online) Simulated (red) and measured (blue) time-of-detection difference histograms for full length of the subframes (a) and close to the prompt region (b) for f_{coarse}.

varying the source-detector distances in the simulation over a range, that was consistent with the spatial distribution of the detected diagram line photons (see Figs. 2 and 3), one obtains $(\Delta\delta_{KK})_{\text{dist.}}/\delta_{KK} \in [-0.025, 0.038]$, $(\Delta\delta_{KL,LK})_{\text{dist.}}/\delta_{KL,LK} \in [-0.017, 0.063]$, $(\Delta\delta_{\text{IB1S}})_{\text{dist.}}/\delta_{\text{IB}} \in [-0.064, 0.060]$.

Uncertainties in the Kapton foil thickness and geometry could have affected δ_{IB}, δ_{KK}, and $\delta_{KL,LK}$. Errors were determined by varying the foil thickness: $(\Delta\delta_{KK})_{\text{thickness}}/\delta_{KK} \in [-0.0470, 0.0488]$, $(\Delta\delta_{KL,LK})_{\text{thickness}}/\delta_{KL,LK} \in [-0.058, 0.115]$, and $(\Delta\delta_{\text{IB}1S})_{\text{thickness}}/\delta_{\text{IB1S}} \in [-0.0005, 0.0046]$.

The value for the source activity which was known with a relative uncertainty of $\Delta A/A = \pm 0.015$ could have influenced the calculation of δ_K. We obtained $(\Delta\delta_K)_A/\delta_K = \Delta A/A = 0.015$ neglecting the statistical fluctuation of the large number N_K. Table I shows the resulting simulated errors obtained for these variables by variation of the underlying parameters.

A numerical simulation has been used to determine the overall statistical and systematic errors of P_{KK} separately. All variables were varied independently and simultaneously according to their Poissonian error (statistical error) or homogeneous probability distribution between minimum and maximum values (systematic errors). All uncertainties given here reflect a confidence level of 68.2%.

In the analysis presented so far, the two detectors were regarded as one single, larger pixel detector which was able to detect coincidences of several particles emitted during double-vacancy production. Additionally, we could also determine P_{KK} separately either by identifying coincidences in two clusters in each single detector (single-sided analysis for $P_{KK,\text{A}}$, $P_{KK,\text{B}}$) or by identifying only coincident clusters between the two detectors (double-sided analysis for $P_{KK,\text{A}\wedge\text{B}}$). Such a separation is only possible with pixel detectors.

For the single-sided analysis, $P_{KK,\text{A}}$ and $P_{KK,\text{B}}$ could be determined using Eq. (16) for the two detectors separately. For each detector, only coincidences of two clusters of triggered pixels in this detector were taken into account. The following quantities were determined separately for each detector in the already described way: the detection yields for satellite photons ($\delta_{\text{A,S}}$, $\delta_{\text{B,S}}$), hypersatellite photons ($\delta_{\text{A,H}}$, $\delta_{\text{B,H}}$), diagram line photons ($\delta_{\text{A,K}}$, $\delta_{\text{B,K}}$), K-shell shake-off electrons ($\delta_{\text{A,KK}}$, $\delta_{\text{B,KK}}$), internal bremsstrahlung photons ($\delta_{\text{A,IB1S}}$, $\delta_{\text{B,IB1S}}$), L-shell shake-off electrons after K capture and K-shell shake-off electrons after L capture $\delta_{\text{A,KL,LK}}$, $\delta_{\text{B,KL,LK}}$, and $\kappa_{\text{A,H}}$, $\kappa_{\text{B,H}}$, $\kappa_{\text{A,S}}$, $\kappa_{\text{B,S}}$, the various correction factors γ for solid angle reduction due to the cut on the distance between clusters, the number of coincidences ($N_{\text{A,Signal}}$, $N_{\text{B,Signal}}$), number of detected diagram line photons ($N_{\text{A,K}}$, $N_{\text{B,K}}$), losses due to accidental vetoes ($P_{\text{A,loss}}$, $P_{\text{B,loss}}$), random coincidences ($N_{\text{A,acc}}$, $N_{\text{B,acc}}$), number of background events ($N_{\text{A,bg,ext}}$, $N_{\text{B,bg,ext}}$).

The result of the single-sided analysis was $P_{KK,\text{A}} = (1.684 \pm 0.150) \times 10^{-4}$ for detector A and $P_{KK,\text{B}} = (1.351 \pm 0.159) \times 10^{-4}$ for detector B. The systematic errors were $(\Delta P_{KK,\text{A}})_{\text{syst}} = \pm 0.026 \times 10^{-4}$ for detector A and $(\Delta P_{KK,\text{B}})_{\text{syst}} = \pm 0.021 \times 10^{-4}$ for detector B. These two values could be combined to $P_{KK,\text{A}\veebar\text{B}} = (1.528 \pm 0.109) \times 10^{-4}$ with a systematic uncertainty of $(\Delta P_{KK,\text{A}\veebar\text{B}})_{\text{syst}} = \pm 0.024 \times 10^{-4}$.

In the derivation of Eq. (16), the whole setup with two pixel detectors was treated like one single pixel detector with an effective detection yield which was the sum of the individual detection yields of the two detectors, for example, $\delta_K = \delta_{\text{A,K}} + \delta_{\text{B,K}}$. This calculation is no longer applicable if P_{KK} shall be extracted from the number of events that triggered both detectors (double-sided analysis) at the same time. The contributions of the five signatures, as defined in the derivation

of Eq. (16), became for the double-sided analysis (A $\wedge$ B)

$$N_{1,\mathrm{A}\wedge\mathrm{B}} = A\ P_K\ \tau\ T\ P_{KK}\ \omega_K^2\ (\delta_{\mathrm{A},H}\delta_{\mathrm{B},S} + \delta_{\mathrm{A},S}\delta_{\mathrm{B},H})\ (1 - \delta_{\mathrm{A},KK} - \delta_{\mathrm{B},KK}), \tag{17}$$

$$N_{2,\mathrm{A}\wedge\mathrm{B}} = A\ P_K\ \tau\ T\ P_{KK}\ \omega_K^2\ (\delta_{\mathrm{A},S}\ \delta_{\mathrm{B},KK} + \delta_{\mathrm{B},S}\ \delta_{\mathrm{A},KK})\ (1 - \delta_{\mathrm{A},H} - \delta_{\mathrm{B},H}), \tag{18}$$

$$N_{3,\mathrm{A}\wedge\mathrm{B}} = A\ P_K\ \tau\ T\ P_{KK}\ \omega_K^2\ (\delta_{\mathrm{A},H}\ \delta_{\mathrm{B},KK} + \delta_{\mathrm{B},H}\ \delta_{\mathrm{A},KK})\ (1 - \delta_{\mathrm{A},S} - \delta_{\mathrm{B},S}), \tag{19}$$

$$N_{4,\mathrm{A}\wedge\mathrm{B}} = A\ P_K\ \tau\ T\ P_{KK}\ \omega_K\ (1 - \omega_K)\ (\delta_{\mathrm{A},H}\ \delta_{\mathrm{B},KK} + \delta_{\mathrm{B,H}}\ \delta_{\mathrm{A},KK}), \tag{20}$$

$$N_{5,\mathrm{A}\wedge\mathrm{B}} = A\ P_K\ \tau\ T\ P_{KK}\ \omega_K\ (1 - \omega_K)\ (\delta_{\mathrm{A},S}\ \delta_{\mathrm{B},KK} + \delta_{\mathrm{B},S}\ \delta_{\mathrm{A},KK}). \tag{21}$$

$N_{\mathrm{Signal,A}\wedge\mathrm{B}}$ then became

$$N_{\mathrm{Signal,A}\wedge\mathrm{B}} = P_{KK}\ \omega_K\ (N_{\mathrm{A},K}\ \beta_{\mathrm{A},K} + N_{\mathrm{B},K}\ \beta_{\mathrm{B},K}) \tag{22}$$

with

$$\beta_{\mathrm{A},K} = \kappa_{\mathrm{A},H}\ \delta_{\mathrm{B},S} - 2\ \delta_{\mathrm{B},KK}\left(\kappa_{\mathrm{A},H}\ \delta_{\mathrm{B},S} + \kappa_{\mathrm{A},S}\ \delta_{\mathrm{B},H} + \kappa_{\mathrm{A},H}\ \delta_{\mathrm{A},S} - \frac{\kappa_{\mathrm{A},S} + \kappa_{\mathrm{A},H}}{2\omega_K}\right) \tag{23}$$

and

$$\beta_{\mathrm{B},K} = \kappa_{\mathrm{B},H}\ \delta_{\mathrm{A},S} - 2\ \delta_{\mathrm{A},KK}\left(\kappa_{\mathrm{B},H}\delta_{\mathrm{A},S} + \kappa_{\mathrm{B},S}\ \delta_{\mathrm{A},H} + \kappa_{\mathrm{B},H}\ \delta_{\mathrm{B},S} - \frac{\kappa_{\mathrm{B},S} + \kappa_{\mathrm{B},H}}{2\omega_K}\right), \tag{24}$$

where

$$\delta_{\mathrm{A},H} = \kappa_{\mathrm{A},H}\ \delta_{\mathrm{A},K}, \quad \delta_{\mathrm{A},S} = \kappa_{\mathrm{A},S}\ \delta_{\mathrm{A},K}, \quad \delta_{\mathrm{B},H} = \kappa_{\mathrm{B},H}\ \delta_{\mathrm{B},K}, \quad \delta_{\mathrm{B},S} = \kappa_{\mathrm{B},S}\ \delta_{\mathrm{B},K}. \tag{25}$$

The number of background events due to internal bremsstrahlung was given by

$$N_{\mathrm{IB,A}\wedge\mathrm{B}} = P_{\mathrm{IB1S}}\ (N_{\mathrm{A},K}\ \delta_{\mathrm{B,IB1S}} + N_{\mathrm{B},K}\ \delta_{\mathrm{A,IB1S}}). \tag{26}$$

The number of background events due to L-shell electron shake-off after K capture and K-shell shake-off electron detection after L capture was given by

$$N_{KL,LK,\mathrm{A}\wedge\mathrm{B}} = P_{KL,LK}\ (N_{\mathrm{A},K}\ \kappa_{A,S}\ \delta_{\mathrm{B},KL,LK} + N_{\mathrm{B},K}\ \kappa_{B,S}\ \delta_{\mathrm{A},KL,LK}). \tag{27}$$

$P_{KK,\mathrm{A}\wedge\mathrm{B}}$ could be calculated in the double-sided analysis as

$$P_{KK,\mathrm{A}\wedge\mathrm{B}} = \frac{\frac{N_{\mathrm{prompt,A}\wedge\mathrm{B}} - N_{\mathrm{acc,A}\wedge\mathrm{B}}}{1 - P_{\mathrm{loss,A}\wedge\mathrm{B}}} - N_{\mathrm{bg,ext,A}\wedge\mathrm{B}} - N_{\mathrm{IB,A}\wedge\mathrm{B}} - N_{KL,LK,\mathrm{A}\wedge\mathrm{B}}}{\omega_K\ (N_{\mathrm{A},K}\ \beta_{\mathrm{A},K} + N_{\mathrm{B},K}\ \beta_{\mathrm{B},K})}. \tag{28}$$

The following quantities were determined with the Monte Carlo simulation: $\kappa_{\mathrm{A,H}}$,$\kappa_{\mathrm{A,S}}$,$\kappa_{\mathrm{B,H}}$,$\kappa_{\mathrm{B,H}}$, $\delta_{\mathrm{A,KL,LK}}$, $\delta_{\mathrm{B,KL,LK}}$, $\delta_{\mathrm{A,IB1S}}$,$\delta_{\mathrm{B,IB1S}}$. The result of the double-sided analysis was $P_{KK,\mathrm{A}\wedge\mathrm{B}} = (1.538 \pm 0.114) \times 10^{-4}$ with a systematic error of $\pm 0.023 \times 10^{-4}$ which agreed with the single-sided analysis and the analysis treating both detectors as one large detector. This demonstrated the internal consistency of our analysis.

With the Z^{-2} dependence of P_{KK} predicted by the Primakoff and Porter theory [19], one can extrapolate our result on ^{55}Fe to the electron-capture decay of ^{54}Mn. Here, Z is the nuclear charge of the mother nucleus. One obtains P_{KK} (^{54}Mn)$= (1.656 \pm 0.085) \times 10^{-4}$. The triple-coincidence P_{KK} measurement of Hindi, White, and Kozub [1] on ^{54}Mn resulted in $P_{KK}(^{54}\mathrm{Mn}) = 2.3^{+0.8}_{-0.5} \times 10^{-4}$. Thus, the ratio of this measured value on ^{54}Mn to the value expected from our result amounts to $1.389^{+0.488}_{-0.310}$ which is almost consistent with 1 on a one-sigma level. The dominant source of uncertainties in this comparison is now the statistical error in the measurement on ^{54}Mn. If $P_{KK}(^{55}\mathrm{Fe})$ previously measured by Campbell *et al.* [2] was extrapolated and compared to $P_{KK}(^{54}\mathrm{Mn})$ measured by Hindi, White, and Kozub [1], the ratio of measured to extrapolated P_{KK} was $1.636^{+0.622}_{-0.434}$ which could be considered to be inconsistent with 1. Thus, our results strengthen the theory of Primakoff and Porter [19] by resolving the discrepancy between measured P_{KK} in the decays of ^{54}Mn and ^{55}Fe.

Nagy and Schupp [7] measured P_{KK} in the decay of ^{65}Zn and obtained $P_{KK}(^{65}\mathrm{Zn}) = (2.2 \pm 0.2) \times 10^{-4}$. Extrapolation of our result on ^{55}Fe to ^{65}Zn gives $P_{KK}(^{65}\mathrm{Zn}) = (1.150 \pm 0.059) \times 10^{-4}$. The result of Campbell *et al.* [2] extrapolated ^{65}Zn gives $P_{KK}(^{65}\mathrm{Zn}) = (0.98 \pm 0.15) \times 10^{-4}$. The ratio of the value measured by Nagy and Schupp [7] to the value extrapolated from our measurement is 1.913 ± 0.2. It is obvious that here the discrepancy between the expected and the measured values remains. Due to the improved statistical error of our experiment, the significance of the discrepancy is even increased. The most probable reason might be found in the measurement of Nagy and Schupp [7] which has been carried out as a two-detector coincidence experiment and therefore might not be immune to K-shell internal conversion of γ rays after the electron-capture decay of ^{65}Zn to excited states of ^{65}Cu.

The asymmetry between the results of the P_{KK} determination with the single-sided analysis where both detectors A and

B were treated separately and the double-sided analysis of our experiment with the two detectors in coincidence is consistent with zero: $(P_{KK,\mathrm{A}\veebar\mathrm{B}} - P_{KK,\mathrm{A}\wedge\mathrm{B}})/(P_{KK,\mathrm{A}\veebar\mathrm{B}} + P_{KK,\mathrm{A}\wedge\mathrm{B}}) = -0.003 \pm 0.051$. This strengthens the assumption made in all measurements of P_{KK} in electron-capture decays that the momenta directions of satellite and hypersatellite photons are independent from each other, i.e., that there is no angular correlation.

IV. CONCLUSION

The double-vacancy creation probability in the electron-capture decay of ^{55}Fe was measured with high statistical and systematic precision. The statistical error was improved significantly with respect to earlier measurements. Our result $P_{KK} = (1.531 \pm 0.079) \times 10^{-4}$ with a systematic error of $(\Delta P_{KK})_{\mathrm{syst}} = \pm 0.023 \times 10^{-4}$ is in agreement with the previously measured values.

The potential of the active-pixel detector Timepix, especially the fine segmentation and the time-stamping capability in each pixel, was demonstrated for a use in a long lasting experiment at the intersection between atomic and nuclear physics. This kind of detectors can not only produce valuable results in accelerator based particle physics experiments, where active-pixel detectors have their roots, but also may help experimentalists in neighboring fields like in atomic and nuclear physics.

The way P_{KK} was determined was complementary to previous measurements because our measurement did not rely on precise energy measurements but used the segmentation of the detector for signal event identification and background rejection. It was the first measurement where a single-sided and double-sided measurement of P_{KK} in one experimental setup was performed. No asymmetry between forward-forward and forward-backward emission of satellite and hypersatellite photon was found for the decay of ^{55}Fe. This finding supports, at least for nuclei with a similar nuclear charge, the assumption of direction-uncorrelated hypersatellite-satellite emission which was made in all earlier P_{KK} measurements in electron-capture decays.

The discrepancy between the measured values of the double-vacancy creation probability in electron-capture decays of ^{55}Fe and ^{54}Mn seems to be resolved with our measurement in combination with the Primakoff-Porter theory [19]. The discrepancy between the measured values of P_{KK} for ^{55}Fe and ^{65}Zn remains clearly visible. We therefore recommend triple coincidence measurements of P_{KK} on ^{65}Zn.

ACKNOWLEDGMENTS

We thank the German metrology institute PTB for manufacturing and calibrating the radioactive source and the Medipix collaboration for the development of the Timepix detector. We are grateful to the Deutsche Forschungsgemeinschaft DFG for supporting T. Gleixner. B. Bergmann has been supported by a Marie Curie Early Initial Training Network Fellowship of the European Community's Seventh Framework Programme under Contract No. (PITN-GA-2011-289198-ARDENT).

[1] M. M. Hindi, C. A. White, and R. L. Kozub, Phys. Rev. C **68**, 014306 (2003).
[2] J. L. Campbell, J. A. Maxwell, and W. J. Teesdale, Phys. Rev. C **43**, 1656 (1991).
[3] G. Charpak, Comptes Rendus **237**, 243 (1953).
[4] R. W. Kiser and W. H. Johnston, J. Am. Chem. Soc. **81**, 1810 (1959).
[5] H. J. Nagy and G. Schupp, Phys. Rev. C **30**, 2031 (1984).
[6] J. P. Briand, P. Chevalier, A. Johnson, J. P. Rozet, M. Tavemier, and A. Touati, Phys. Lett. A **49**, 51 (1974).
[7] H. J. Nagy and G. Schupp, Phys. Rev. C **27**, 2887 (1983).
[8] J. P. Briand, P. Chevallier, M. Tavernier, and J. P. Rozet, Phys. Rev. Lett. **27**, 777 (1971).
[9] G. Schupp and H. J. Nagy, Phys. Rev. C **29**, 1414 (1984).
[10] Hyun Jae Cho, Seung Kook Ko, Sang Kyun Nha, Woon Hyuk Chung, Dae Won Lee, Woo Young Ro, and Dal Gyu Ha, J. Korean Phys. Soc. **32**, 123 (1998).
[11] C. W. E. van Eijk, J. Wijnhorst, and M. A. Popelier, Phys. Rev. A **20**, 1749 (1979).
[12] C. W. E. van Eijk, J. Wijnhorst, and M. A. Popelier, Phys. Rev. C **19**, 1047 (1979).
[13] P. A. Indira, I. J. Unus, P. Venugopala Rao, and R. W. Fink, J. Phys. B: At., Mol. Opt. Phys. **12**, 1351 (1979).
[14] M. M. Hindi and R. L. Kozub, Phys. Rev. C **45**, 1070 (1992).
[15] Y. Isozumi, Ch. Briancon, and R. J. Walen, Phys. Rev. C **25**, 3078 (1982).
[16] M. M. Hindi and R. L. Kozub, Phys. Rev C **43**, 461 (1991).
[17] C. W. E. van Eijk, J. P. Wagenaar, F. Bergsma, and W. Lourens, Phys. Rev. A **26**, 2749 (1982).
[18] Hyun Jae Cho and Sang Kyun Nha, J. Korean Phys. Soc. **30**, 521 (1997).
[19] H. Primakoff and F. T. Porter, Phys. Rev. **89**, 930 (1953).
[20] E. P. Kanter, I. Ahmad, R. W. Dunford, D. S. Gemmell, B. Krässig, S. H. Southworth, and L. Young, Phys. Rev. A **73**, 022708 (2006).
[21] P. Cermak, I. Stekl, Yu A. Shitov, F. Mamedov, E. N. Rukhadze, J. M. Jose, J. Cermak, N. I. Rukhadze, V. B. Brudanin, and P. Loaiza, JINST **6**, C01057 (2011).
[22] X. Llopart, R. Ballabriga, M. Campbell, E. H. M. Heijn, L. Tlustos, and W. Wong, Nucl. Instrum. Methods Phys. Res., Sect. A **581**, 485 (2007).
[23] M.-M. Bé, V. Chisté, C. Dulieu, E. Browne, C. Baglin, V. Chechev, N. Kuzmenco, R. Helmer, F. Kondev, D. MacMahon, and K. B. Lee, Table of Radionuclides (Vol. 3), Bureau international des poids et mesures, Monographie BIPM-5, 5-9, 2006 (unpublished).
[24] W. Shockley, J. Appl. Phys. **9**, 635 (1938).
[25] S. Ramo, Proc. IRE **27**, 584 (1939).
[26] X. Llopart, M. Campbell, R. Dinapoli, D. San Segundo, and E. Pernigotti, IEEE Trans. Nucl. Sci. **NS-49**, 2279 (2003).
[27] M. Campbell, Nucl. Instrum. Methods Phys. Res., Sect. A **633**, S1 (2011).
[28] V. Kraus, M. Holik, J. Jakubek, M. Kroupa, P. Soukup, and Z. Vykydal, JINST **6**, C01079 (2011).

[29] T. Holy, J. Jakubek, S. Pospisil, J. Uher, D. Vavrik, and Z. Vykydal, Nucl. Instrum. Methods Phys. Res., Sect. A **563**, 254 (2006).
[30] V. Gromov, M. van Beuzekom, R. Kluit, F. Zappon, V. Zivkovic, M. Campbell, T. Poikela, X. Llopart, C. Brezina, K. Desch, X. Fang, and A. Kruth, PoS (Vertex 2011) 046.
[31] J. Giersch, A. Weidemann, and G. Anton, Nucl. Instrum. Methods Phys. Res., Sect. A **509**, 151 (2003).
[32] H. Spieler and E. Haller, IEEE Trans. Nucl. Sci. **32**, 419 (1985).
[33] P. Sievers, T. Weber, T. Michel, J. Klammer, L. Büermann, and G. Anton, J. Instrum. **7**, P03003 (2012).
[34] D. Mitra, M. Sarkar, D. Bhattacharya, and L. Natarajan, X-Ray Spectrom. **37**, 585 (2008).
[35] J. G. Pengra and B. Crasemann, Phys. Rev. **131**, 2642 (1963).
[36] M. C. Chon and J. Law, Phys. Rev. A **50**, 1372 (1994).
[37] M. Wolfsberg, Phys. Rev. **96**, 1712 (1954).
[38] J. S. Levinger, Phys. Rev. **90**, 11 (1953).
[39] J. C. Slater, Phys. Rev. **36**, 57 (1930).
[40] T. Mukoyama, Bull. Inst. Chem. Res., Kyoto Univ. **63**, 24 (1985).
[41] M. C. P. Isaac, V. R. Vanin, and O. A. M. Helene, Z. Phys. A **335**, 243 (1990).
[42] M. H. Biavati, S. J. Nassif, and C. S. Wu, Phys. Rev. **125**, 1364 (1962).
[43] P. C. Martin and R. J. Glauber, Phys. Rev. **109**, 1307 (1958).
[44] T. Michel, J. Durst, and J. Jakubek, Nucl. Instrum. Methods Phys. Res., Sect. A **603**, 384 (2009).